Salt-templated transformation of waste plastics into single-atom catalysts for environmental and energy applications

Shiying Ren[1], Xin Xu [1], Kunsheng Hu[1], Shuang Zhong [1], Yingjie Gao[1], Bernt Johannessen [2], Wei Ren[1], Hongyu Zhou [1], Zhong-Shuai Zhu[1], Yidi Chen [1,3], Xiaoguang Duan [1] ✉ & Shaobin Wang [1] ✉

Upcycling plastic waste into single-atom catalysts (SACs) not only offers a sustainable solution for plastic waste management but also yields valuable functional materials for catalytic applications. Here, we report a simple and scalable method to transform various types of plastics, including polyethylene, polypropylene, polystyrene, polyethylene terephthalate, polyvinyl chloride, and their mixtures, into a diversity of porous SACs with different coordination chemistry and their excellent applications in a variety of catalytic reactions. Lamellar transition metal chloride salts (Ni, Fe, Co, Mn, and Cu) are employed as a template and catalyst for confined carbonization of plastics into layered SACs. An appropriate plastic-to-salt ratio is the key factor for preventing metal agglomeration during SAC synthesis. The SACs demonstrate exceptional catalytic activity in oxidative degradation of a range of persistent organic pollutants for water treatment and excel in electrocatalytic systems such as oxygen/nitrogen reduction reactions and lithium-sulfur batteries. This technique provides a versatile, scalable, and efficient strategy for upcycling solid wastes into high-performance materials for environmental and energy catalysis.

Plastics, a major component of municipal waste, pose escalating environmental burdens due to their widespread use and non-biodegradability. The ongoing accumulation of plastic waste in the world has driven the pursuit of sustainable strategies for recycling and upgrading these plastics into value-added products. Five most common plastics, polyethylene (PE), polystyrene (PS), polypropylene (PP), polyethylene terephthalate (PET), and polyvinyl chloride (PVC), contain approximately 85.7%, 85.7%, 92.3%, 62.5%, and 38.7% carbon by mass, respectively. The carbon-rich nature makes plastics promising precursors for upcycling into functional carbonaceous materials. Indeed, a variety of approaches have been proposed for converting plastic waste into graphene[1–4], carbon nanotubes[5–8], carbon spheres[9–12], carbon nanosheets[13–15], and porous carbon[16–18]. Global demand for graphene and graphite is projected to reach about $2.1 and $27 billion

by 2025, respectively[19,20]. Converting waste plastics into high-value carbonaceous products thus provides a sustainable alternative to their conventional landfill disposal and incineration, while reducing carbon emissions and promoting a plastic-based circular economy.

Single-atom catalysts (SACs) have emerged as cutting-edge catalysts that bridge the gap between homogeneous and heterogeneous catalysis[21]. They offer exceptional catalytic performance through maximizing atomic metal utilization, unique electronic properties, and high specific surface areas (SSAs). In SACs, metal active sites are typically atomically dispersed and coordinated by hetero-non-metal atoms (often nitrogen) in carbon matrixes, providing superior structural stability and resistance to agglomeration in diverse catalytic processes[22]. Recently, SACs have been extensively explored for different catalytic applications, including persulfate-based advanced

[1]School of Chemical Engineering, The University of Adelaide, Adelaide, SA, Australia. [2]Australian Synchrotron, ANSTO, Victoria, VIC, Australia. [3]State Key Laboratory of Urban Water Resource and Environment, Shenzhen Key Laboratory of Organic Pollution Prevention and Control, School of Civil and Environmental Engineering, Harbin Institute of Technology, Shenzhen, PR China. ✉e-mail: xiaoguang.duan@adelaide.edu.au; shaobin.wang@adelaide.edu.au

oxidation processes (PS-AOPs) for wastewater treatment, owing to their strong activity and capacity to facilitate both radical and non-radical pathways. Moreover, their electronic structures can be precisely regulated at the molecular level to meet the requirements of specific redox reactions[23–26]. Despite these advantages, a low product yield of pyrolysis-derived carbon-based SACs remains a significant bottleneck toward large-scale applications[27,28], largely due to a substantial mass loss during the rapid vaporization of the small molecules decomposed from polymer degradation.

Transforming plastic wastes into high-value SACs not only mitigates plastic pollution but also supplies high-performance catalysts for catalytic applications. However, several key challenges persist in direct plastics-to-SACs conversion: (1) lack of a universal, scalable method capable of fabricating SACs from diverse plastics and their mixtures; (2) limited plastics-to-carbon conversion efficiency under pyrolysis conditions; (3) uniformly incorporate target metal atoms into a carbon matrix to achieve critical catalytic functionality while preventing metal aggregation; (4) complexity of the mechanisms that govern plastic transformation and SAC formation.

In this work, we developed a universal method to construct a comprehensive SAC library from PE, PP, PS, PET, PVC, and mixed plastics (MPs). Metal chloride salts (Ni, Fe, Co, Mn, and Cu) were employed as both graphitization catalysts and structure templates during plastic transformation processes to secure a high product yield and surface area of the obtained SACs. An ammonia gaseous environment afforded spontaneous nitrogen doping to anchor the metallic atoms into the carbon network to form uniformly dispersed metal sites as SACs. We subsequently demonstrated the superior performances of these SACs in PS-AOPs for degrading various water pollutants via catalytic persulfate activation, as well as in electrochemical applications such as oxygen reduction reactions, nitrogen reduction to ammonia, and Li-S batteries. Overall, this work represents a substantial advance in integrating plastic waste management with SAC manufacturing, highlighting the promise of converting solid wastes into valuable catalysts for safeguarding water quality, energy conversion, and sustainability.

Results

Universality of the synthesis in plastics-derived SACs

Figure 1a illustrates the procedure of SAC synthesis from various plastics and metal chloride salts. Plastics were mixed with transition metal chloride salts at specific mass ratios and pyrolyzed at 800 °C for 3 h under an ammonia atmosphere. The resulting mixture was purified through hydrochloric acid pickling, yielding SAC products. During the synthesis, plastics were first pyrolyzed into light hydrocarbons (350–500 °C, including gas and oil)[29]. The metal chloride catalyzes the transformation of these light hydrocarbons into a graphitic network between the salt lattices, thus acting as both catalysts and templates during plastic carbonization[26]. The introduction of a metal salt into mixed plastics substantially reduced gas yields and intensified carbonization (Supplementary Fig. S1). Supplementary Fig. S2 shows that the addition of cobalt chloride also accelerated the conversion of medium-chain hydrocarbons (C16–C20) to long-chain hydrocarbons (C23–C30) and short-chain gaseous products (C2–C4). Simultaneously, partial metal species from the salt interacted with ammonia-derived nitrogen dopants and generated atomically dispersed metal sites into the carbon matrix. Spontaneously, some chloride ions from the metal salts were also integrated into the metal coordination environment, forming a featured metal-N_4-Cl configuration. Figure 1b presents the obtained SACs synthesized from different plastics and metal salts, demonstrating the universality of the approach in transforming different types of plastics and MPs into SACs. As shown in Fig. 1a, c single-batch synthesis of CuSA-PE achieved a product yield of 1.1 g in a lab-scale tube furnace, suggesting promising potential for large-scale production of SACs from plastics.

Scanning electron microscopy (SEM) images of various SACs derived from different plastics are shown in Supplementary Fig. S3. Notable different morphologies were observed on the surface of car-
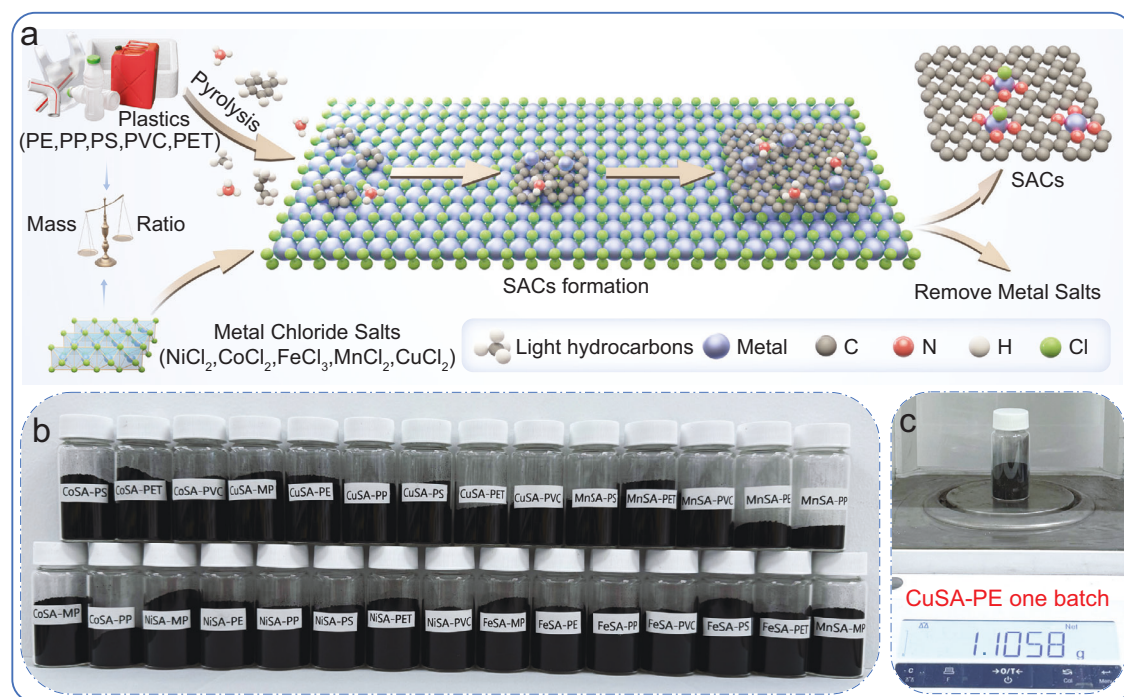

Fig. 1 | Synthesis and showcase of plastic-derived SACs. a Schematic illustration of single-atom catalysts (SACs) derived from plastics and transition metal salts. PE refer to polyethylene, PP refer to polypropylene, PS refer to polystyrene, PET refer to polyethylene terephthalate, PVC refer to polyvinyl chloride. **b** Image of various SACs synthesized from different plastics and metal salts. **c** The product yield of CuSA-PE synthesized from PE and copper chloride in one batch.
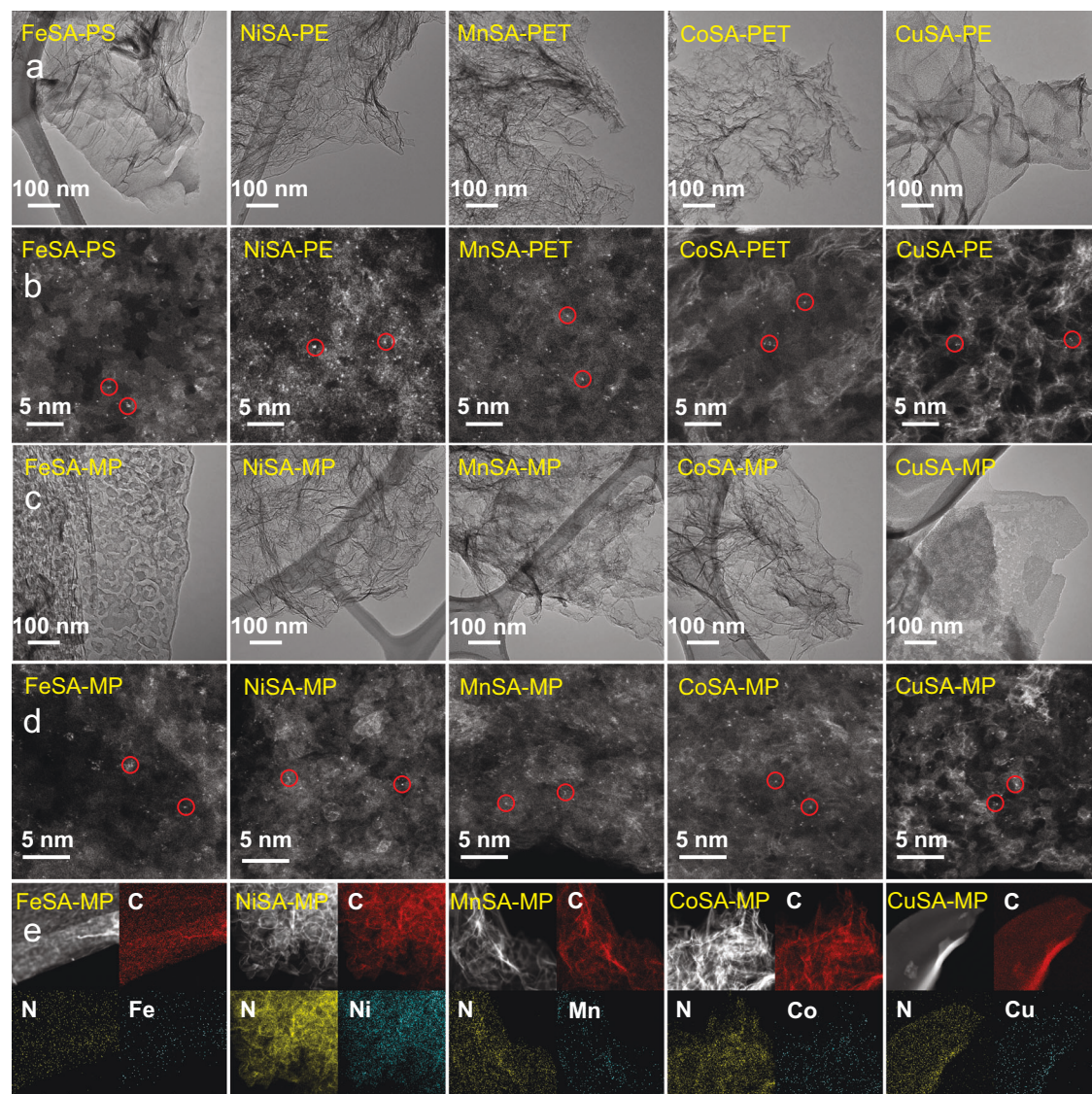
Fig. 2 | Microscopic characterizations of plastic-derived SACs. a TEM images of five SACs derived from single-type plastics. **b** HAADF-STEM images of five SACs derived from single-type plastics and single atoms are circled in red. **c** TEM images of five SACs derived from mixed plastics (MPs). **d** HAADF-STEM images of five SACs derived from MPs and single atoms are circled in red. **e** HAADF-STEM and the corresponding EDS mapping images of five SACs derived from MPs. The scale bar is 500 nm.

bon products, including corrugated lamellar structures (Ni, Mn, and Co SACs), thick sheets (Cu SACs), and bulk/layered features (Fe SACs). These distinct morphologies of SACs may be attributed to the intrinsic crystal structures and melting points of the corresponding metal salt templates. As shown in Supplementary Table S1, the trigonal crystal structure with high melting points for $NiCl_2$, $CoCl_2$, and $MnCl_2$ tended to form corrugated lamellar nanocarbons. In contrast, the $FeCl_3$ trigonal crystal structure with a low melting point (306 °C) facilitated confined carbonization to yield bulk or layered features. The monoclinic crystal structure with a relatively low melting point for $CuCl_2$ was inclined to produce flat lamellar nanocarbon. X-ray diffraction (XRD) patterns of SACs before acid pickling (Supplementary Fig. S4) exhibit metal chloride peaks, indicating their template role during the plastic transformation. After hydrochloric acid pickling, the XRD patterns of diverse SACs (Supplementary Fig. S5) presented a prominent (002) carbon peak at $2\theta = 26°$, while no discernible impurity peak was observed (except for MnSA-PE, MnSA-PP, and NiSA-PVC), confirming that most metal salts were successfully removed. The metal loadings of all plastic-derived SACs are below 1 wt% (Supplementary Table S2).

Transition electron microscopy (TEM) images of the five transition metal SACs derived from different types of plastics in Fig. 2a depict that all the SACs displayed lamellar structures. High-angle annular dark-field scanning transmission electron microscopy (HAADF-STEM) images in Fig. 2b further demonstrate the uniform dispersion of metal single atoms in the carbon matrix for each plastic-derived SAC. In addition, MPs (with a mass ratio of PE: PP: PS: PET: PVC = 1:1:1:1:1) were also successfully transformed into SACs using the same salt template approach. The TEM and HAADF-STEM images (Fig. 2c, d) display that all MPs-derived SACs exhibit atomically dispersed metal sites in the lamellar carbon matrix. Energy-dispersive X-ray spectroscopy (EDS) mapping images in Fig. 2e further confirm the homogeneous distributions of C, N, and metal atoms in MPs-derived SACs.

We further found that a mass ratio of plastics to metal chloride salts critically affects both the product yield and structure of SACs. The product yield and XRD patterns (Supplementary Figs. S6–S10) of samples synthesized at varying mass ratios indicate that excessive plastics or metal chloride salts resulted in a low product yield or
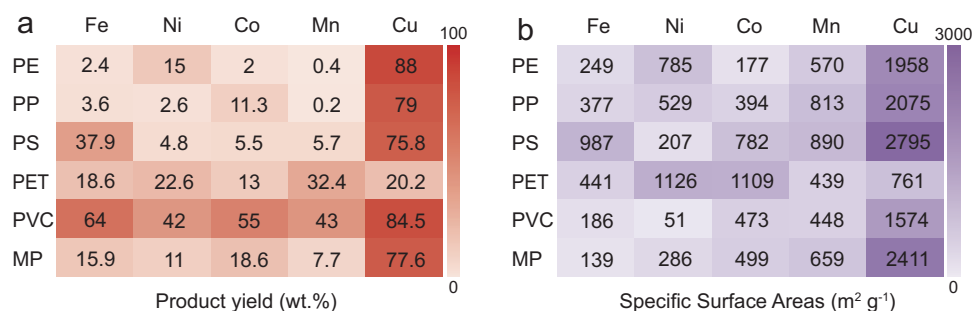
Fig. 3 | Product yield and specific surface areas of plastic-derived SACs. a Product yield and **b** SSAs of various SACs synthesized from different plastics and metal salts. The color depth represents the numerical magnitudes of product yield and specific surface areas.

impurities in the carbon products that could not be removed by hydrochloric acid. Hence, optimizing the mass ratio was essential to effectively transform different plastics into SACs, and the optimal mass ratios were summarized in Supplementary Table S3. In the optimal mass ratio, metal chloride was always excessive because the formation of nanocarbons with a lamellar structure needed excessive metal chloride to act as templates.

The SAC product yield and carbon conversion efficiency (by mass) were summarized in Fig. 3a and Supplementary Fig. S11 to evaluate the impact of categories of metals and plastics on conversion efficiency. Because of low metal loadings, SAC product yields and corresponding carbon conversion efficiency were almost identical. Notably, the product yield of Cu SACs was significantly higher than other transition metals, with CuSA-PE achieving the highest product yield at 88%. The exceptional yield of Cu SACs was due to the lower solubility of carbon in solid Cu[30,31], resulting in the flat growth of graphene on the Cu surface (Supplementary Fig. S3e). In contrast, the relatively higher solubility of carbon in other transition metals led to the formation of corrugated carbons (Supplementary Figs. S3b–d). The flat growth mode was conducive to maximum interaction between decomposed plastic molecules and active Cu surface, leading to subsequent extensive in-plane carbon extension, thereby increasing the carbon yield. Among the various plastics, PVC displayed a considerably higher product yield than other plastics, possibly owing to the formation of chlorinated ethylene with activated C–C bonds that are conducive to the carbonization process.

Nitrogen sorption and desorption isotherms of various SACs are depicted in Supplementary Figs. S12–S16. Their corresponding total pore, micropore, and mesopore volumes as well as SSAs are included in Fig. 3b and Supplementary Fig. S17. Notably, CuSA-PS exhibited the highest SSA (2795 $m^2 g^{-1}$) and micropore volume (1.12 $cm^3 g^{-1}$), whereas MnSA-PE showed the highest pore volume (9.16 $cm^3 g^{-1}$) and mesopore volume (8.94 $cm^3 g^{-1}$). The influence of different transition metals on the pore structures of SACs is illustrated in Supplementary Fig. S18. Cu SACs generally exhibited significantly higher SSAs (Supplementary Fig. S18a) and micropore volumes (Supplementary Fig. S18c) compared to other metal-based SACs, implying that Cu promoted the formation of micropores during plastic transformation, which in turn accounts for the large SSAs. Conversely, Mn and Ni SACs presented larger total pores (Supplementary Fig. S18b) and mesopore volumes (Supplementary Fig. S18d) than other metal-based SACs, illustrating that Mn and Ni tend to convert plastics into mesoporous structures. These mesopores primarily contributed to the overall pore volume due to the existence of larger void spaces. Supplementary Fig. S19 shows the impact of plastic types on pore formation. PS-derived SACs exhibited higher SSAs (Supplementary Fig. S19a) and micropore volumes (Supplementary Fig. S19c), whereas PP- and PE-derived SACs displayed higher total pore (Supplementary Fig. S19b) and mesopore volumes (Supplementary Fig. S19d). These findings suggest that PS precursors preferred to form micropores, while PP and PE were

inclined to produce mesopores. The I_D/I_G ratios of each plastic-derived SACs calculated from the corresponding Raman spectra were all close to 1 (Supplementary Figs. S20–S24 and Supplementary Table S4), indicating that most SACs exhibited similar graphitic structures. In summary, the characterizations demonstrated the universality of this salt-templating approach for upcycling various plastics into SACs with high quality and controlled physicochemical properties.

Universality in the electronic and coordination environments

Synchrotron soft X-ray spectroscopy (SXRS) was employed to elucidate the chemical configuration of the synthesized SACs. The carbon K-edge spectra of various SACs in Supplementary Fig. S25a exhibited three peaks at 285.3 (peak π), 288.2 (peak N-M), and 292.6 eV (peak σ). The π and σ peaks arise from the dipole transition of the C 1s core electron to π* C=C and σ* C–C orbitals[32]. The N-M peak signifies the formation of C-N-metal bonds in the carbon matrix[33,34]. Supplementary Fig. S25b depicts the nitrogen K-edge spectra of various SACs. Ni, Mn, and Cu SACs presented three prominent peaks at 397.8, 400.9, and 407 eV, corresponding to pyridinic, pyrrolic, and graphitic nitrogen, respectively[34,35]. In contrast, Fe and Co SACs displayed only two peaks corresponding to pyrrolic and graphitic nitrogen, suggesting differences in the nitrogen coordination environments across different metal centers. The metal L-edge spectra (Supplementary Fig. S25c) further revealed the oxidation states of the metal single sites in the synthesized SACs. Mn SACs exhibited mixed valence states of Mn^{2+} and Mn^{3+}, located at 639.5 and 640.8 eV, respectively[36]. Other SACs predominantly displayed a +2 oxidation state, including Fe^{2+} at 708.5 eV, Ni^{2+} at 851.4 eV, Co^{2+} at 778 eV, and Cu^{2+} at 929.9 eV[37–39]. Lastly, the Cl L-edge spectra (Supplementary Fig. S25d) present a peak at 204 eV in Fe, Ni, Mn, Co SACs, and CuSA-PET, indicating that Cl was selectively functionalized into these SACs.

X-ray absorption near-edge spectroscopy (XANES), and extended X-ray absorption structure (EXAFS) analyses provide high-resolution insights into the electronic and coordination structures of SACs[40–43]. The metal K-edge XANES spectra in Supplementary Fig. S26 reveal that the MPs-derived SACs exhibit identical features to their corresponding metal phthalocyanine (MPc), indicating their comparable D_{4h} symmetry. Specifically, FePc, NiPc, CoPc, and CuPc present significant peaks at 7117, 8338, 7715, and 8986 eV, respectively, which correspond to the 1s → $4p_z$ electron transition and the square-planar metal-N coordination[44]. The vanished 1s → $4p_z$ transition peak in MPs-derived SACs revealed their modified metal coordination environment with distorted D_{4h} symmetric geometry[45]. Supplementary Fig. S27 shows that most single type plastics-derived SACs (except for Mn-PP and Co-PP) exhibit similar features to their corresponding MPs-derived SACs, indicating their similar coordination environment. Fourier-transformed (FT) EXAFS spectra of various SACs and references are displayed in Figs. 4a, b. The FT peak was observed at 2.2 Å for metal-metal bonding in Ni-PVC and Co-PE exclusively, implying the presence of metallic clusters or nanoparticles in these catalysts. By contrast, all
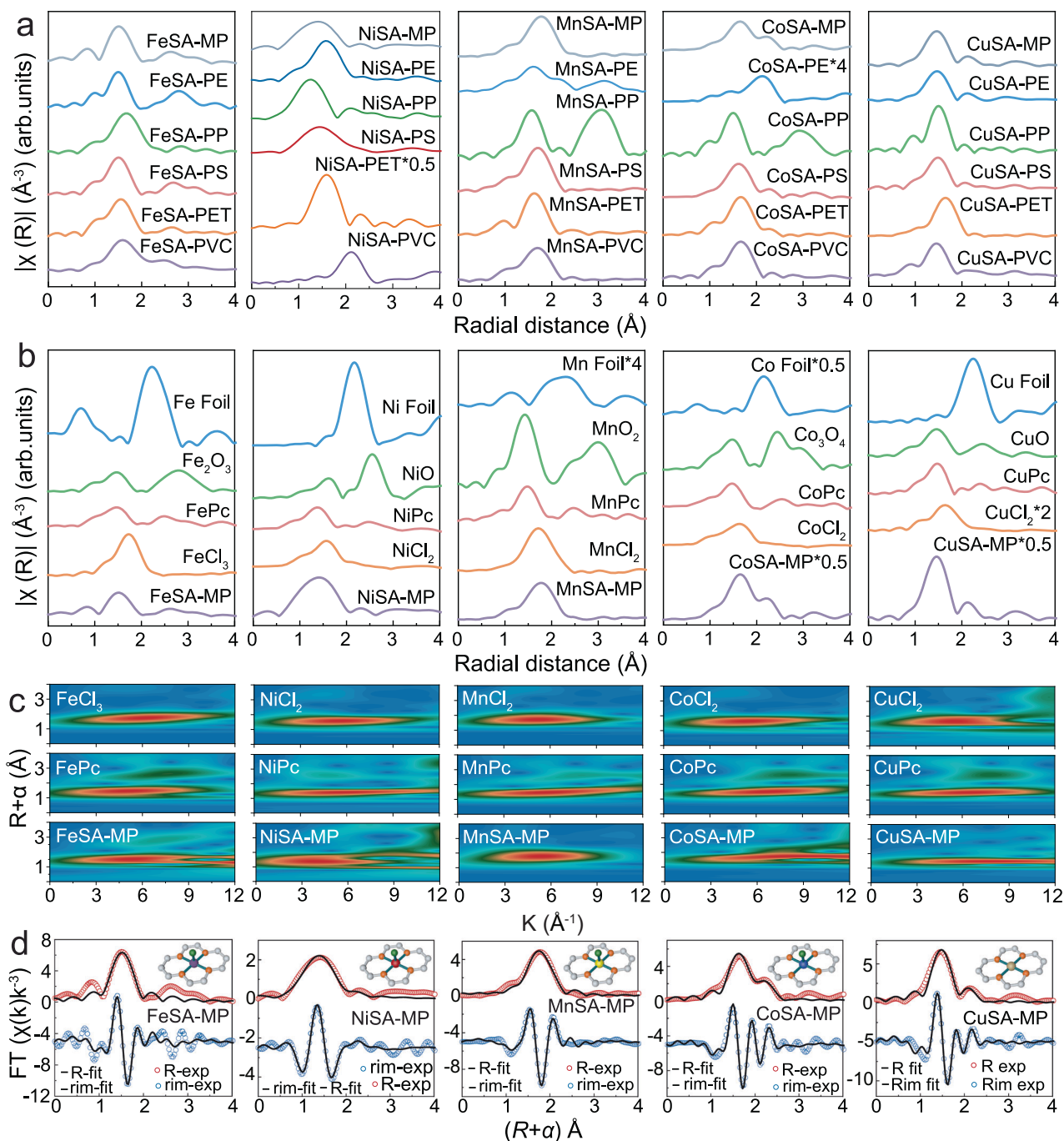
Fig. 4 | Synchrotron characterizations of plastic-derived SACs. a Fourier-transformed extended X-ray absorption structure (FT-EXAFS) spectra in R space of diverse SACs synthesized from different plastics and metal salts. **b** The comparison of FT-EXAFS spectra in R space between MPs-derived SACs and various metallic references (metal foils, metal oxides, metal phthalocyanine (Pc), and metal chlorides). **c** Wavelet Transform (WT)-EXAFS plots of MPs-derived SACs, metal phthalocyanine, and metal chloride. **d** The FT-EXAFS R space fitting spectra of various SACs synthesized from MPs and the inset figure is the molecular model of each MP-SAC.

other SACs exhibited peaks at 1.4–1.7 Å without the peak at 2.2 Å, confirming that metal sites primarily existed in an isolated state. The wavelet transform (WT) contour plots of the MPs-derived SACs and metal references (Fig. 4c) further supported the single atom features of these obtained SACs. Quantitative EXAFS curve fitting analysis (Fig. 4d, Supplementary Figs. S28–S32, and Tables S5–S9) disclosed that most plastics-derived Cu SACs (apart from CuSA-PET) exhibited $Cu-N_4$ coordination structure and other metal-based SACs (Fe, Co, Ni, Mn) all showed Metal-N_4-Cl coordination structure (Supplementary Table S10). The Cl L-edge spectra in Supplementary Fig. S33 reveal a

distinct Cl signal in NiSA-PE, while no Cl signal is observed in Carbon-HDPE, confirming that Cl was not incorporated into the carbon framework of Carbon-HDPE. Given that Cl^- is a bulky monodentate ligand, in-plane incorporation would induce significant steric repulsion with neighboring N and C in the carbon framework. Consequently, Cl^- preferentially occupies the axial position of metal, which minimizes the steric hindrance and electronic repulsion, leading to a more energetically favorable geometry, such as a square-pyramidal or distorted trigonal bipyramidal configuration[46–48]. In addition, Cl coordination in the axial position exhibited much lower formation energy
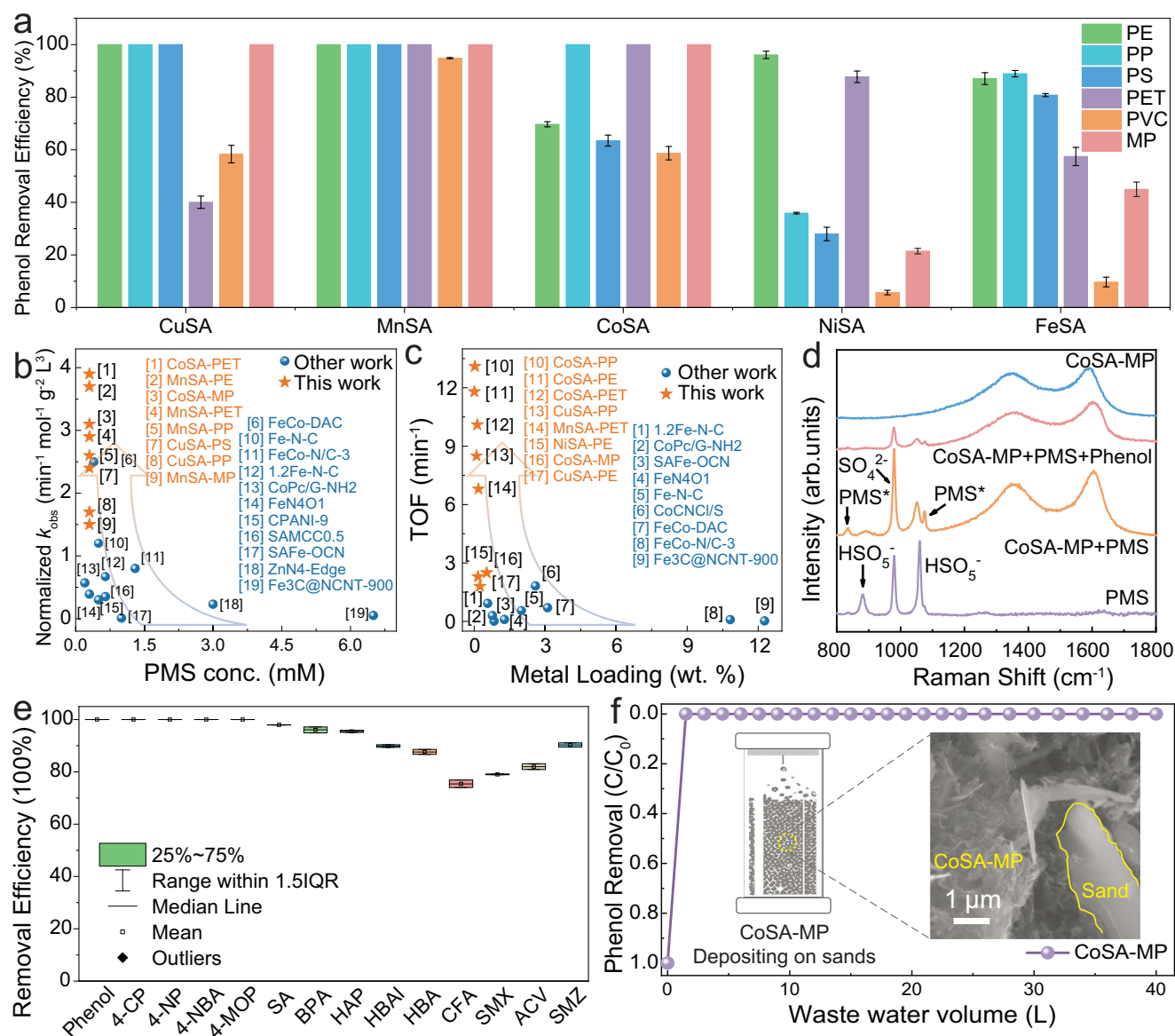
Fig. 5 | Catalytic efficiency of plastic-derived SACs in waste water treatment. **a** Phenol removal efficiency of diverse plastic-derived SACs. **b** Normalized kinetic rate constants of phenol removal for SACs synthesized from different methods. **c** Comparison of TOF values and metal loading for state-of-the-art Fenton-like SACs. **d** In-situ Raman spectra. **e** Removal efficiency of various pollutants in CoSA-MP/PMS system in 30 min. **f** The stability test of the CoSA-MP + PMS oxidation system and the illustration of CoSA-MP depositing on sand (inset). Experimental conditions: (**a**–**e** without **d**) [catalyst] = 0.05 g L^{-1}, [PMS] = 0.3 mM, [Pollutant] = 0.1 mM. **d** [catalyst] = 1 g L^{-1}, [PMS] = 100 mM, [Phenol] = 100 ppm. (f) [PMS] = 0.3 mM, [Phenol] = 2 ppm, [catalyst] = 200 mg. The error bars in Fig. 5a,e refer to the standard deviations (mean values ± s.d., n = 2), obtained by repeating the experiment at least twice.

than the in-plane incorporation[49]. The unique coordination environment of Cu SACs likely stemmed from the fully electron-filled 3d orbitals of the Cu atom, which preferred to construct the Cu-N$_4$ coordination without Cu−Cl interactions. Overall, SXRS and XANES analyses demonstrated that the metal atoms in most plastics-derived SACs were anchored to the carbon substrate through nitrogen binding with an in-plane Metal-N$_4$ coordination.

Performance evaluation of plastic-derived SACs
The catalytic performance of the plastics-derived SACs was first evaluated in PS-AOPs. As shown in Supplementary Fig. S34, the effect of peroxymonosulfate (PMS) dosage on phenol removal demonstrated that phenol could be completely removed in 10 min at PMS dosage exceeding 0.3 mM (PMS:phenol = 3:1). Further increases in PMS concentration did not improve the degradation efficiency, because all catalytic metal sites have been occupied. Therefore, 0.3 mM PMS was

selected to evaluate the catalytic performance of the plastics-derived SACs in phenol oxidation (Fig. 5a and Supplementary Fig. S35). Among the 30 tested samples, 12 SACs achieved 100% phenol degradation within 30 min with PMS activation. Supplementary Fig. S36a, b show that PS- and PET-derived SACs and Cu-based SACs displayed higher phenol adsorption, attributed to their substantial SSAs and micropore volumes. Furthermore, CoSA-PET, MnSA-PE, CoSA-MP, MnSA-PET, and MnSA-PP exhibited extremely higher kinetic rate constants (k_{obs}) (0.58 min^{-1}, 0.56 min^{-1}, 0.47 min^{-1}, 0.44 min^{-1}, and 0.39 min^{-1}, respectively) than other SACs (Supplementary Fig. S37). Their dosage-normalized k_{obs} (Fig. 5b) and turnover frequency (TOF, Fig. 5c) outperformed most SACs synthesized from other methods (Supplementary Table S11). Supplementary Fig. S38 highlights the impact of plastic and metal types on k_{obs}, illustrating that PET-derived SACs and Mn-based SACs possessed the highest catalytic efficiency, followed by Co and Cu SACs. Conversely, PVC-derived SACs exhibited relatively low

activity in PMS activation. The distinct catalytic performances between SACs using the same metal while different plastics are correlated to the specific surface area (SSA) and defect degree (I_D/I_G) of each SAC, which was verified by the linear relationship (Supplementary Fig. S39) between dosage-normalized k_{obs} and SSA, I_D/I_G normalized k_{obs} (per active site k_{obs}). These findings suggest that upcycling plastics into high-activity Mn-, Co-, and Cu-based SACs provides a viable strategy for effective catalysts to drive rapid oxidation of organic pollutants in AOPs.

As real-life plastic wastes commonly consist of multiple plastic types, MPs-based SACs hold a greater promise in practical applications. Among them, CoSA-MP exhibited the highest PMS activation efficiency and relatively low pollutant adsorption, making it ideal for mechanistic studies of catalytic PMS activation and pollutant oxidation. As shown in Supplementary Fig. S40, the negligible inhibiting effect of typical radical scavengers (methanol, ethanol, and 2,2,6,6-tetramethyl-4-piperidinol (TEMP)) and insignificant oxidation effect on benzoic acid and nitrobenzene in the CoSA-MP/PMS system excluded the involvement of hydroxyl/sulfate radicals (•OH and $SO_4^{•-}$) or $^1O_2$ in the phenol oxidation[15,50–52]. Electron paramagnetic resonance (EPR) analysis only detected 5,5-dimethyl-1-pyrroline N-oxide (DMPOX), a direct oxidation product of 5,5-dimethyl-1-pyrroline N-oxide (DMPO), while no radical adduct was observed, indicating a non-radical oxidation pathway (Supplementary Fig. S41a)[53]. The flat signal in Supplementary Fig. S41b further confirmed the absence of $^1O_2$, as no TEMP adduct was detected[54]. Furthermore, CoSA-MP did not enhance the oxidation of methyl phenyl sulfoxide (PMSO) or increase methyl phenyl sulfone ($PMSO_2$) formation (Supplementary Fig. S42a). The $PMSO_2$ yield was even lower than the direct PMS oxidation without a catalyst (Supplementary Fig. S42b), indicating that $Co^{IV}=O$ was not generated in the CoSA-MP + PMS system[26]. These findings collectively suggest that free radicals, $^1O_2$, and $Co^{IV}=O$ were not the dominant reactive species in the CoSA-MP/PMS system.

In-situ Raman spectroscopy was conducted to investigate the interactions between CoSA-MP and PMS (Fig. 5d). The PMS solution presented three characteristic peaks at 980 (SO_4^{2-}), 879 and 1060 cm^{-1} (HSO_5^-). The addition of CoSA-MP introduced two new peaks at 835 and 1074 cm^{-1}, indicating the formation of surface-confined intermediates (PMS*). These new peaks weakened upon the addition of phenol, suggesting that the PMS* behaved as a non-radical reactive species involved in pollutant oxidation[55]. In-situ Fourier transform infrared spectroscopy (FTIR) spectra (Supplementary Fig. S43) of PMS solution exhibited characteristic peaks at 1060, 1105, and 1260 cm^{-1}, corresponding to the S=O stretching vibration of HSO_5^-, S-O stretching vibration of SO_4^{2-}, and HSO_5^-, respectively[49,56]. Upon introduction of CoSA-MP, the peaks at 1060 and 1260 cm^{-1} red-shifted to 1051 and 1200 cm^{-1}, respectively, indicating the generation of PMS* intermediates. Following the phenol addition, these peaks reverted to 1060 and 1260 cm^{-1}, indicating instant PMS* consumption for phenol oxidation[57].

Open circuit potential curves (Supplementary Fig. S44a) further illustrate that the addition of PMS resulted in a substantial potential increase, which stabilized at 1.015 V, indicating that the formation of the PMS*-SAC complex led to a raised oxidation potential. After the introduction of phenol, the potential decreased, confirming that PMS* accepted electrons from phenol (electron donor) via the carbon surface, verifying the electron-transfer process (ETP) in the CoSA-MP/PMS system. The current-time curve (Supplementary Fig. S44b) provided additional insight into these interactions. When the CoSA-MP electrode was applied a 1.015 V potential (matching the equilibrium potential of PMS* in the open circuit potential), the current experienced a sharp drop from 1×10^{-4} to 2×10^{-6} µA. Upon phenol addition, the current instantly increased to 6.4×10^{-6} µA and then gradually decreased to 4.6×10^{-6} µA, confirming that the CoSA-MP serves as the electron shuttle to transfer electrons from phenol and surface-

activated PMS* during the oxidation process[58]. To verify the ETP regime, we constructed a galvanic oxidation setup (GOS, Supplementary Fig. S45a), using CoSA-MP-coated graphite paper as both electrodes. PMS and phenol solutions were placed in separate cells, bridged by a proton exchange membrane and an ammeter. The CoSA-MP + GOS system (Supplementary Fig. S45b) displayed a sharp current (2.8 mA) and 100% phenol removal, while the GOS system with bare graphite paper electrode as the control group showed minimal activity (0.3 mA, ~6%). These results confirm CoSA-MP served as both an activator and electron mediator to trigger an ETP regime for spontaneous PMS activation (electron acceptor) and pollutant oxidation (charge donor). A metal-poisoning experiment in Supplementary Fig. S46 depicts that phenol removal efficiency was significantly reduced upon ethylenediaminetetraacetic acid (EDTA) or potassium thiocyanate (KSCN) addition, indicating that Co single atoms are the primary catalytic sites for PMS activation[59].

The CoSA-MP/PMS system achieved a total organic carbon (TOC) reduction from 8.35 to 0.78 mg L^{-1}, corresponding to ~90% carbon removal (Supplementary Fig. S47). Surface product extraction and ultrahigh performance liquid chromatography-mass spectrometry (HPLC-MS) analysis (Supplementary Fig. S48a) revealed that the major surface species were dimeric and trimeric phenoxyls (Supplementary Fig. S48b). A proposed polymerization pathway (Supplementary Fig. S49) involves PMS*-mediated electron abstraction from phenol at the hydroxy group, ortho, and para positions, thus generating organic radicals. These radicals undergo C–C and C–O coupling to form different oligomers, and some may undergo hydroxylation or oxidation to quinone-containing polymers[60,61].

Natural water systems contain various inorganic ions (such as Cl$^-$, SO_4^{2-}, NO_3^-) and humic acid (HA), which normally influence the performance of AOPs[62–64]. The impacts of these background factors and real water matrixes were also evaluated. Supplementary Fig. S50 demonstrated that these ions and practical water matrix had minimal impacts on phenol degradation in the CoSA-MP/PMS system, suggesting the resilience of the CoSA-MP/PMS system to fulfill the remediation task in practical water treatment. Harsh conditions, such as extreme solution pH typically limited the application of conventional metal-based AOPs[65,66]. The post-reaction solution was analyzed by inductively coupled plasma mass spectrometry (ICP-MS), and the Co concentration was only 1.3 ppb, demonstrating the structural stability of single-atom Co in CoSA-MP. Nevertheless, as illustrated in Supplementary Fig. S51, the CoSA-MP/PMS system maintained 100% phenol removal efficiency across a wide pH range (3 to 11, initial pH control and pH buffer condition), demonstrating the structural robustness of plastics-derived SACs during the catalytic oxidation process. Furthermore, the CoSA-MP/PMS system achieved over 70% removal efficiency within 30 min for a variety of organic pollutants (Fig. 5e and Supplementary Figs. S52 and S53), including phenol, 4-chlorophenol (4-CP), 4-aminophenol (4-NP), 4-aminobenzoic acid (4-NBA), 4-methoxyphenol (4-MOP), sulfanilamide (SA), bisphenol A (BPA), 4-hydroxyacetophenone (HAP), 4-hydroxybenzaldehyde (HBAl), 4-hydroxybenzoic acid (HBA), 2-(4-chlorophenoxy)−2-methylpropionic acid (CFA), sulfamethoxazole (SMX), acyclovir (ACV), and sulfamerazine (SMZ). The long-term practical water treatment (Supplementary Fig. S54) of phenol was investigated in a fixed-bed reactor packed with CoSA-MP and sands (the inset of Fig. 5f). The system continually treated 40 L wastewater and maintained 100% phenol removal (Fig. 5f), implying the high purification efficiency and stability of the CoSA-MP + PMS system.

Moreover, the plastics-derived SACs also exhibited excellent performances in typical electrochemical systems, such as nitrogen reduction reaction (NRR) to yield ammonia, oxygen reduction reaction (ORR), and lithium-sulfur (Li-S) batteries. Supplementary Fig. S55 illustrates that CuSA-PE showed a high current density and Faraday efficiency for NH_4^+ formation (78%), implying its excellent NRR

catalytic performance. The negligible current fluctuation over a 12 h operation further demonstrated the stability of CuSA-PE[67]. In the electrochemical ORR measurements (Supplementary Fig. S56), MnSA-PET and CuSA-MP exhibited high onset potential of (0.9 and 0.86 V, respectively) and relatively low H_2O_2 selectivity (11% and 8% at 0 V), indicating that they preferred the 4e⁻ ORR pathway to reduce O_2 to H_2O[68]. In contrast, NiSA-PE and NiSA-MP illustrated a high peroxide oxidation current on the ring electrode (0.09 and 0.08 mA) and high H_2O_2 selectivity (86% and 73%), suggesting that they proceeded toward the 2e⁻ pathway[69].

In addition, when equipped in a Li-S battery, the galvanostatic discharge profiles of the plastics-derived SACs-based sulfur cathodes exhibited elevated and extended discharge plateaus (Supplementary Fig. S57a), reflecting enhanced reduction kinetics from sulfur to polysulfides. Notably, S/NiSA-PE, S/CoSA-PET, and S/MnSA-PET electrodes achieved initial discharge capacities of 1175, 1012, and 1011 mAh g⁻¹, respectively, outperforming the reference S/CNT (908 mAh g⁻¹). This improved catalytic activity was further corroborated by the positive shift in cathodic peaks and the higher, sharper redox currents observed in cyclic voltammetry (Supplementary Fig. S57b). Furthermore, the S/NiSA-PE electrode maintained a significantly higher discharge capacity of 770 mAh g⁻¹ after 100 cycles, compared to 620 mAh g⁻¹ for S/CNT (Supplementary Fig. S58), demonstrating its superior long-term electrochemical stability and performance for a Li-S battery.

Discussion

In this study, we have established a facile and universal approach for transforming various plastic wastes into SACs, providing a sustainable solution for the upcycling of plastic wastes into state-of-the-art functional materials for catalytic applications. Optimizing the salt-to-plastic mass ratio is critical for preventing metal aggregation and ensuring atomic dispersion during SAC synthesis. Notably, the approach realized gram-scale fabrication of SACs from plastics in a single batch in a laboratory furnace and functionalized the SACs with diverse SAC coordination sites and large SSAs. The versatility in processing various plastics and their mixtures highlights the broad applicability of this approach in real-world applications. The plastics-derived SACs demonstrated superior performance in catalytic oxidation of organic pollutants at low dosage of PMS consumption and triggered a non-radical ETP regime that can remediate a broad spectrum of contaminants. Plastics-derived SACs also exhibit excellent activity in electrochemical reactions. The wise upcycling of plastics into advanced materials will contribute to a circular economy in plastic management, catalysis, and beyond.

Methods
Synthesis of diverse SACs from plastics
Commercial plastics were first cut into small pieces using a blender. These plastic fragments were then mixed with a specific metal chloride salt at defined mass ratios and dissolved in 200 mL of ethanol. The mixture was stirred at 70 °C until ethanol fully evaporated, producing a precipitate. The precipitate was transferred to a tube furnace, where it was annealed at 210 °C for 1 h, followed by heating at 800 °C for 3 h under an ammonia atmosphere. The obtained mixture was ground into powder and purified in 2.4 M hydrochloric acid, stirring for 48 h at 60 °C to thoroughly remove the metal impurities. The product was filtered and washed with ultrapure water until the solution reached neutral pH 7. The purified carbon materials were dried in an oven at 60 °C for 2 days. The dried carbon samples were then named according to the type of metal, plastic, and plastics-to-metal mass ratio, such as Co-MP-1/5, Cu-PE-1/40, Mn-PET-1/5, Fe-PVC-1/10, and Ni-PP-1/1. The optimized SACs were further designated based on the metal and plastics with the addition of "SA", such as FeSA-PE, NiSA-PP, and CoSA-MP. Carbon-HDPE was produced using the same synthesis

procedure as NiSA-PE but under an Ar atmosphere. The product yield was calculated by the following equation.

$$\eta = mass(SAC)/[mass(plastics)*Q(carbon)] \quad (1)$$

Where, η is the product yield of SACs, mass (SAC) is the weight of the obtained SAC, mass (plastics) is the weight of plastics, and Q (carbon) is the weight percentage of the carbon element in the plastics.

Material characterizations
The morphologies of carbon samples were characterized by scanning electron microscopy (SEM, SU 7000) and transmission electron microscopy (TEM, Tecnai G2 Spirit 120 kV). HAADF images and elemental mapping were conducted on the FEI Titan Themis 80–200. In-situ Raman spectra were performed on a Raman spectrometer (Horiba LabRAM HR Evolution) with a 532 nm green laser. X-ray diffraction (XRD) analysis was conducted on a Rigaku MiniFlex 600. The specific surface areas of carbon samples were measured using the Brunauer−Emmett−Teller (BET) method from N_2 adsorption−desorption isotherms (V-Sorb 2800 P, Ultrametrics). The X-ray absorption data were collected on the X-ray absorption spectroscopy (XAS) and soft X-ray spectroscopy (SXRS) beamline at Australian Synchrotron (Melbourne). All X-ray absorption spectra were measured in a transition mode at room temperature.

Catalytic performance of carbon materials in AOPs
Phenol (or other organic pollutants, 0.1 mM) was dissolved into 50 mL ultrapure water, followed by adding 0.05 g L⁻¹ catalyst. After 10 min pre-adsorption, 0.3 mM PMS (or a specified amount) was added. The solution samples were periodically withdrawn using a syringe equipped with a 0.22 μm filter. All degradation tests were performed at 25 °C with constant stirring at 800 rpm. The pseudo-first-order kinetic rate constants were calculated by the following equation.

$$\ln(C/C_0) = -k_{obs}t \quad (2)$$

Where, C_0 is the initial organic concentration, C is the organic concentration at time t, and k_{obs} is the reaction rate constant.

During the quenching experiments, radical scavengers and pollutants were introduced into the solution prior to the addition of catalysts, following the same procedures used in the degradation tests. Inorganic ions were added after phenol to evaluate the impact of actual water matrices, and the other procedures were consistent with the quenching tests. To test the effect of solution pH, we adjusted the pH by 0.5 mM H_2SO_4 and NaOH after the addition of phenol, and the other experiment steps remained the same as in the quenching tests. The concentration of organics was analyzed using ultrahigh performance liquid chromatography (HPLC, Ultimate 3000, Thermo Scientific) with a C-18 column. HPLC analytical conditions for different pollutants are summarized in Supplementary Table S12.

Data availability
The processed data generated in this study are provided in the main text, supplementary information, and Source Data files. Additional data are available from the corresponding author upon request. Source data are provided with this paper.

References
1. Wyss, K. M. et al. Synthesis of clean hydrogen gas from waste plastic at zero net cost. *Adv. Mater.* **35**, 2306763 (2023).
2. Cui, L., Wang, X., Chen, N., Ji, B. & Qu, L. Trash to treasure: converting plastic waste into a useful graphene foil. *Nanoscale* **9**, 9089–9094 (2017).
3. Algozeeb, W. A. et al. Flash graphene from plastic waste. *ACS Nano* **14**, 15595–15604 (2020).

4. Sun, Z. et al. Growth of graphene from solid carbon sources. *Nature* **468**, 549–552 (2010).

5. Wyss, K. M. et al. Upcycling of waste plastic into hybrid carbon nanomaterials. *Adv. Mater.* **35**, 2209621 (2023).

6. Tang, T., Chen, X., Meng, X., Chen, H. & Ding, Y. Synthesis of multiwalled carbon nanotubes by catalytic combustion of polypropylene. *Angew. Chem. Int. Ed.* **44**, 1517–1520 (2005).

7. Jie, X. et al. Microwave-initiated catalytic deconstruction of plastic waste into hydrogen and high-value carbons. *Nat. Catal.* **3**, 902–912 (2020).

8. Liu, Q. et al. Pyrolysis–catalysis upcycling of waste plastic using a multilayer stainless-steel catalyst toward a circular economy. *Proc. Natl. Acad. Sci. USA* **120**, e2305078120 (2023).

9. Lu, A. H. et al. Synthesis of discrete and dispersible hollow carbon nanospheres with high uniformity by using confined nanospace pyrolysis. *Angew. Chem. Int. Ed.* **50**, 11765–11768 (2011).

10. Gong, J. et al. Converting mixed plastics into mesoporous hollow carbon spheres with controllable diameter. *Appl. Catal. B Environ.* **152–153**, 289–299 (2014).

11. Pol, V. G. Upcycling: converting waste plastics into paramagnetic, conducting, solid, pure carbon microspheres. *Environ. Sci. Technol.* **44**, 4753–4759 (2010).

12. Sawant, S. Y., Somani, R. S., Panda, A. B. & Bajaj, H. C. Utilization of plastic wastes for synthesis of carbon microspheres and their use as a template for nanocrystalline copper(II) oxide hollow spheres. *ACS Sustain. Chem. Eng.* **1**, 1390–1397 (2013).

13. Gong, J. et al. Converting real-world mixed waste plastics into porous carbon nanosheets with excellent performance in the adsorption of an organic dye from wastewater. *J. Mater. Chem. A* **3**, 341–351 (2015).

14. Ma, C. et al. Sustainable recycling of waste polystyrene into hierarchical porous carbon nanosheets with potential applications in supercapacitors. *Nanotechnology* **31**, 035402 (2020).

15. Ren, S. et al. Catalytic transformation of microplastics to functional carbon for catalytic peroxymonosulfate activation: conversion mechanism and defect of scavenging. *Appl. Catal. B Environ.* **342**, 123410 (2024).

16. Algozeeb, W. A. et al. Plastic waste product captures carbon dioxide in nanometer pores. *ACS Nano* **16**, 7284–7290 (2022).

17. Ma, C. et al. Transforming polystyrene waste into 3D hierarchically porous carbon for high-performance supercapacitors. *Chemosphere* **253**, 126755 (2020).

18. Min, J. et al. A general approach towards carbonization of plastic waste into a well-designed 3D porous carbon framework for super lithium-ion batteries. *Chem. Commun.* **56**, 9142–9145 (2020).

19. Sinha, A. & So, H. Structural effects of crumpled graphene and recent developments in comprehensive sensor applications: a review. *Small Struct.* **4**, 2300084 (2023).

20. Reiss, T., Hjelt, K. & Ferrari, A. C. Graphene is on track to deliver on its promises. *Nat. Nanotechnol.* **14**, 907–910 (2019).

21. Shan, J. et al. Metal-metal interactions in correlated single-atom catalysts. *Sci. Adv.* **8**, eabo0762 (2022).

22. Han, L. et al. A single-atom library for guided monometallic and concentration-complex multimetallic designs. *Nat. Mater.* **21**, 681–688 (2022).

23. Wu, X. & Kim, J.-H. Outlook on single atom catalysts for persulfate-based advanced oxidation. *ACS EST Engg.* **2**, 1776–1796 (2022).

24. Huang, B. et al. Modulating electronic structure engineering of atomically dispersed cobalt catalyst in Fenton-like reaction for efficient degradation of organic pollutants. *Environ. Sci. Technol.* **57**, 14071–14081 (2023).

25. Cheng, C. et al. Generation of Fe^{IV}=O and its contribution to Fenton-like reactions on a single-atom iron–N–C catalyst. *Angew. Chem. Int. Ed.* **135**, e202218510 (2023).

26. Wu, Q.-Y., Yang, Z.-W., Wang, Z.-W. & Wang, W.-L. Oxygen doping of cobalt-single-atom coordination enhances peroxymonosulfate activation and high-valent cobalt–oxo species formation. *Proc. Natl. Acad. Sci. USA* **120**, e2219923120 (2023).

27. Wang, S., Wang, L., Wang, D. & Li, Y. Recent advances of single-atom catalysts in CO_2 conversion. *Energy Environ. Sci.* **16**, 2759–2803 (2023).

28. Yang, Y. et al. Recent progress of carbon-supported single-atom catalysts for energy conversion and storage. *Matter* **3**, 1442–1476 (2020).

29. Ren, S. et al. Structure-oriented conversions of plastics to carbon nanomaterials. *Carbon Res.* **1**, 15 (2022).

30. López, G. A. & Mittemeijer, E. J. The solubility of C in solid Cu. *Scr. Mater.* **51**, 1–5 (2004).

31. Luo, D. et al. Adlayer-free large-area single crystal graphene grown on a Cu(111) foil. *Adv. Mater.* **31**, 1903615 (2019).

32. Han, G.-F. et al. Building and identifying highly active oxygenated groups in carbon materials for oxygen reduction to H_2O_2. *Nat. Commun.* **11**, 2209 (2020).

33. Tong, Y. et al. A bifunctional hybrid electrocatalyst for oxygen reduction and evolution: cobalt oxide nanoparticles strongly coupled to B,N-decorated graphene. *Angew. Chem. Int. Ed.* **56**, 7121–7125 (2017).

34. Shang, H. et al. Engineering unsymmetrically coordinated $Cu\text{-}S_1N_3$ single atom sites with enhanced oxygen reduction activity. *Nat. Commun.* **11**, 3049 (2020).

35. Li, K. et al. Atomic tuning of single-atom Fe–N–C catalysts with phosphorus for robust electrochemical CO_2 reduction. *Nano Lett.* **22**, 1557–1565 (2022).

36. Späth, A. Additive nano-lithography with focused soft X-rays: basics, challenges, and opportunities. *Micromachines* **10**, 834 (2019).

37. Dou, J. et al. Photochemical degradation of iron(III) citrate/citric acid aerosol quantified with the combination of three complementary experimental techniques and a kinetic process model. *Atmos. Chem. Phys.* **21**, 315–338 (2021).

38. Meyers, D. et al. Zhang-Rice physics and anomalous copper states in A-site ordered perovskites. *Sci. Rep.* **3**, 1834 (2013).

39. Ying, B. et al. Monitoring the formation of nickel-poor and nickel-rich oxide cathode materials for lithium-ion batteries with synchrotron radiation. *Chem. Mater.* **35**, 1514–1526 (2023).

40. Xie, X. et al. Performance enhancement and degradation mechanism identification of a single-atom Co–N–C catalyst for proton exchange membrane fuel cells. *Nat. Catal.* **3**, 1044–1054 (2020).

41. Li, J. et al. Identification of durable and non-durable FeN_x sites in Fe–N–C materials for proton exchange membrane fuel cells. *Nat. Catal.* **4**, 10–19 (2021).

42. Zhang, S. et al. Atomically dispersed bimetallic Fe–Co electrocatalysts for green production of ammonia. *Nat. Sustain.* **6**, 169–179 (2022).

43. Wang, A., Li, J. & Zhang, T. Heterogeneous single-atom catalysis. *Nat. Rev. Chem.* **2**, 65–81 (2018).

44. Yang, H. et al. Atomically dispersed Ni(I) as the active site for electrochemical CO_2 reduction. *Nat. Energy* **3**, 140–147 (2018).

45. Ren, X. et al. In-situ spectroscopic probe of the intrinsic structure feature of single-atom center in electrochemical CO/CO_2 reduction to methanol. *Nat. Commun.* **14**, 3401 (2023).

46. Qiao, Z., Jiang, R., Xu, H., Cao, D. & Zeng, X. C. A general descriptor for single-atom catalysts with axial ligands. *Angew. Chem. Int. Ed.* **136**, e202407812 (2024).

47. Liu, M. et al. In situ modulating coordination fields of single-atom cobalt catalyst for enhanced oxygen reduction reaction. *Nat. Commun.* **15**, 1675 (2024).

48. Qiao, J. et al. Spin engineering of Fe—N—C by axial ligand modulation for enhanced bifunctional oxygen catalysis. *Adv. Funct. Mater.* **34**, 2409794 (2024).

49. Ren, S. et al. Transforming plastics to single atom catalysts for peroxymonosulfate activation: axial chloride coordination intensified electron transfer pathway. *Adv. Mater.* **37**, 2415339 (2025).

50. Chen, X., Oh, W., Da & Lim, T. T. Graphene- and CNTs-based carbocatalysts in persulfates activation: material design and catalytic mechanisms. *Chem. Eng. J.* **354**, 941–976 (2018).

51. Li, Y. et al. Uniform N-coordinated single-atomic iron sites dispersed in porous carbon framework to activate PMS for efficient BPA degradation via high-valent iron-oxo species. *Chem. Eng. J.* **389**, 124382 (2020).

52. Lee, H. et al. Activation of persulfates by graphitized nanodiamonds for removal of organic compounds. *Environ. Sci. Technol.* **50**, 10134–10142 (2016).

53. Duan, X. et al. Insights into N-doping in single-walled carbon nanotubes for enhanced activation of superoxides: a mechanistic study. *Chem. Commun.* **51**, 15249–15252 (2015).

54. Tian, W. et al. Enhanced removals of micropollutants in binary organic systems by biomass derived porous carbon/peroxymonosulfate. *J. Hazard. Mater.* **408**, 124459 (2021).

55. Ren, W. et al. Hydroxyl radical dominated elimination of plasticizers by peroxymonosulfate on metal-free boron: kinetics and mechanisms. *Water Res.* **186**, 116361 (2020).

56. Beattie, D. A., Chapelet, J. K., Gräfe, M., Skinner, W. M. & Smith, E. In situ ATR FTIR studies of SO_4 adsorption on goethite in the presence of copper ions. *Environ. Sci. Technol.* **42**, 9191–9196 (2008).

57. Mo, Y. et al. Metal- and site-specific roles of high-entropy spinel oxides in catalytic oxidative polymerization of water contaminants. *ACS Catal.* **15**, 5928–5942 (2025).

58. Ren, W. et al. Origins of electron-transfer regime in persulfate-based nonradical oxidation processes. *Environ. Sci. Technol.* **56**, 78–97 (2022).

59. Chen, J., Zhou, X., Sun, P., Zhang, Y. & Huang, C.-H. Complexation enhances Cu(II)-activated peroxydisulfate: a novel activation mechanism and Cu(III) contribution. *Environ. Sci. Technol.* **53**, 11774–11782 (2019).

60. Yao, Z. et al. High-entropy alloys catalyzing polymeric transformation of water pollutants with remarkably improved electron utilization efficiency. *Nat. Commun.* **16**, 148 (2025).

61. Duan, P.-J. et al. Polymeric products deactivate carbon-based catalysts in catalytic oxidation reactions. *Nat. Water* **3**, 178–190 (2025).

62. He, X. & O'Shea, K. E. Selective oxidation of H_1-antihistamines by unactivated peroxymonosulfate (PMS): influence of inorganic anions and organic compounds. *Water Res.* **186**, 116401 (2020).

63. Wang, J. & Wang, S. Effect of inorganic anions on the performance of advanced oxidation processes for degradation of organic contaminants. *Chem. Eng. J.* **411**, 128392 (2021).

64. Hu, L., Zhang, G., Liu, M., Wang, Q. & Wang, P. Enhanced degradation of bisphenol A (BPA) by peroxymonosulfate with Co_3O_4-Bi_2O_3 catalyst activation: effects of pH, inorganic anions, and water matrix. *Chem. Eng. J.* **338**, 300–310 (2018).

65. Peng, Y. et al. Thermodynamic and kinetic behaviors of persulfate-based electron-transfer regime in carbocatalysis. *Environ. Sci. Technol.* **57**, 19012–19022 (2023).

66. Wang, Q. et al. Degradation of bisphenol a using peroxymonosulfate activated by single-atomic cobalt catalysts: different reactive species at acidic and alkaline pH. *Chem. Eng. J.* **439**, 135002 (2022).

67. Xie, F. et al. A general approach to 3D-printed single-atom catalysts. *Nat. Synth.* **2**, 129–139 (2023).

68. Chang, Q. et al. Promoting H_2O_2 production via 2-electron oxygen reduction by coordinating partially oxidized Pd with defect carbon. *Nat. Commun.* **11**, 2178 (2020).

69. Zhang, C. et al. A pentagonal defect-rich metal-free carbon electrocatalyst for boosting acidic O_2 reduction to H_2O_2 production. *J. Am. Chem. Soc.* **145**, 11589–11598 (2023).

Author contributions

S.R., X.D., and S.W. designed the research. S.R. completed most of the experiments and wrote the paper. X.D. and S.W. supervised the research and further revised the paper. X.X., K.H., S.Z., Y.G., B.J., W.R., H.Z., Z.Z. and Y.C. performed data analysis and some characterizations. All authors discussed the results and commented on the paper.

Competing interests

The authors declare no competing interests.

Additional information

Supplementary information The online version contains supplementary material available at https://doi.org/10.1038/s41467-025-63648-z.

Correspondence and requests for materials should be addressed to Xiaoguang Duan or Shaobin Wang.

Peer review information *Nature Communications* thanks Weiming Zhang, and the other anonymous reviewer(s) for their contribution to the peer review of this work. A peer review file is available.

Reprints and permissions information is available at http://www.nature.com/reprints

Publisher's note Springer Nature remains neutral with regard to jurisdictional claims in published maps and institutional affiliations.